

Research on Aerodynamic-Structural Rapid Evaluation and Optimization Methods for Joined-Wing Configurations

Xiao TANG[1,2], Baigang MI[1,2]

[1]School of Aeronautics, Northwestern Polytechnical University, Xi'an 710072, China
[2]National Key Laboratory of Aircraft Configuration Design, Xi'an 710072, China

Abstract

Joined-wing aircraft form a spatial load-carrying system through the front wing, rear wing and end plates, and therefore have potential advantages in reducing induced drag, improving structural efficiency and providing multidirectional space for mission payload integration. However, this configuration involves strong aerodynamic interference, structural static indeterminacy and aeroelastic coupling during conceptual and preliminary design. Directly relying on high-fidelity Computational Fluid Dynamics (CFD), structural Finite Element Method (FEM) and coupled simulations for parametric design and optimization would lead to prohibitive computational cost. To address this issue, this paper develops a two-way coupled aerodynamic-structural rapid evaluation method for the preliminary design of the main lifting surfaces of joined-wing configurations. The aerodynamic model is based on the Vortex Lattice Method (VLM). A non-penetration boundary condition is imposed along the local normal direction of the deformed lifting surface, so that sweep, camber, geometric twist and elastic deformation are consistently included in the circulation solution. Meanwhile, two-dimensional lift-curve-slope correction, friction drag, pressure drag, sweep-related drag correction and the Viterna-Corrigan post-stall model are introduced to compensate for the inviscid and attached-flow assumptions of the conventional VLM. For structural analysis, an Equivalent Plate Model is established to describe the two-dimensional stiffness contribution of the skin, spars, ribs and flange strips in the wing box. The aerodynamic loads and structural deformation are transferred on a shared mesh to form a quasi-static two-way coupling framework. The proposed rapid evaluation model is validated against CFD data for a simplified single-wing model under different leading-edge sweep angles and angles of attack, and against FEM results for structural deflection. The results show that the mean relative errors of lift, drag and lift-to-drag ratio over 45 CFD comparison cases are 2.69%, 3.45% and 5.29%, respectively, while the relative error of the maximum structural deflection is approximately 2.19%. These results indicate that the model can provide sufficient accuracy for trend prediction and parameter screening in preliminary design. Based on this model, an aerodynamic-structural multi-objective optimization framework using NSGA-II is further formulated, where the lift-to-drag ratio and structural weight are taken as the main objectives and high-fidelity verification of representative Pareto solutions is considered.

Keywords: Joined-Wing Aircraft, Fluid-Structure Coupling, VLM, EPM, MDO

1. General Introduction

High-altitude long-endurance unmanned platforms impose integrated requirements on aerodynamic efficiency, structural weight, mission-payload installation space and flight stability. Compared with conventional aircraft layouts, the joined-wing configuration forms a three-dimensional spatial frame through the front wing, rear wing and end plates, which can alleviate the stiffness deficiency of high-aspect-ratio wings and reduce induced drag to some extent. Therefore, the joined-wing layout is

regarded as a promising configuration for long-endurance reconnaissance, patrol and multi-mission payload integration[1-2,15].

Nevertheless, the design of joined-wing aircraft is a typical multidisciplinary coupling problem. Aerodynamically, the front wing, rear wing and end plates interact with each other, and the local load distribution and wing-tip vortex structure differ from those of conventional aircraft. Structurally, the end plates connecting the front and rear wings alter the load-transfer path and boundary constraints, making bending, torsion and local deformation strongly coupled. During conceptual and preliminary design, performing high-fidelity CFD, FEM or fluid-structure interaction simulations for every candidate configuration would significantly reduce the efficiency of parametric design and multi-objective optimization[2-3,16-17].

Low-order physics-based models are of great value in preliminary aircraft design. The vortex lattice method can predict the circulation distribution, lift and induced-drag trends of finite lifting surfaces at low computational cost[3-5]. The equivalent plate model can retain the two-dimensional stiffness characteristics of a wing box with relatively few degrees of freedom[8]. However, the conventional VLM is based on inviscid, incompressible potential-flow assumptions and cannot accurately describe skin-friction drag, pressure drag and separated stall. In recent years, curved-surface VLM and unsteady VLM have been widely used in static aeroelastic analysis of flexible and high-aspect-ratio wings. These studies commonly apply the non-penetration boundary condition on the local normal direction of the deformed aerodynamic surface, so that the fluid velocity is zero in the surface-normal direction[6-7,18-19]. This indicates that, for wings with camber, sweep, twist and significant elastic deformation, a complete local-normal boundary condition is more physically consistent than a simplified downwash condition in the global z direction.

This paper aims to construct an aerodynamic-structural rapid evaluation model that supports two-way fluid-structure coupling and can be embedded into an optimization process. Since a complete joined-wing configuration would simultaneously introduce front/rear-wing interference, end-plate interference drag and fuselage effects, this work first establishes a simplified wing model for the key load-carrying lifting surface of the joined-wing aircraft, so as to verify the basic accuracy and correction strategy of the rapid aerodynamic-structural evaluation model.

The main contributions of this paper are as follows: a quasi-three-dimensional VLM model is established with hybrid cosine meshing, sweep, camber, elastic deformation and geometric twist; an aerodynamic correction strategy combining VLM and strip theory is introduced; an equivalent plate structural model is developed; a two-way coupled aerodynamic-structural rapid evaluation model is built and validated against CFD data; and an NSGA-II-based aerodynamic-structural multi-objective optimization framework is formulated.

2. Research Object and Hierarchical Modelling Strategy

As shown in Figure 1, the joined-wing configuration features front/rear-wing connection and multiple load paths. If a complete joined-wing rapid evaluation model is established before the component models are sufficiently verified, aerodynamic-interference errors, structural-equivalence errors and coupling-transfer errors would appear simultaneously, making it difficult to identify the dominant source of error. Therefore, a simplified single-wing model is first established with reference to the front-wing span, root chord, tip chord and leading-edge sweep angle of the target joined-wing aircraft. A hierarchical modelling strategy is adopted. First, the simplified single-wing model is used to improve the VLM aerodynamic prediction, equivalent plate structural representation and aerodynamic-

structural coupling framework. Second, the model is extended to a simplified two-wing configuration including the front and rear wings, so that the prediction accuracy of the main lifting surfaces can be verified. Finally, fuselage effects, overall geometric constraints and mission-payload constraints will be incorporated into the multidisciplinary optimization framework.

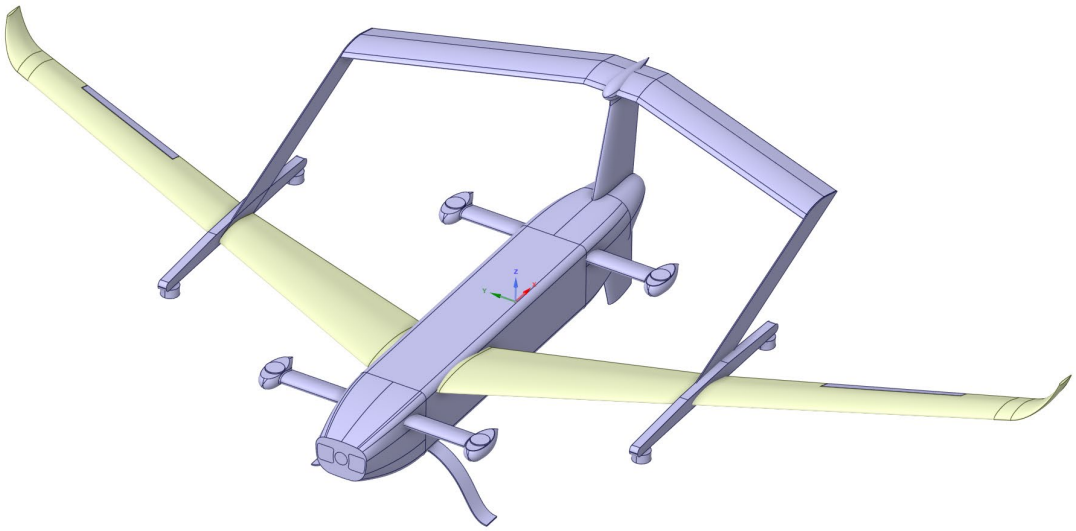


Figure 1 – Schematic of the integrated joined-wing aircraft

This hierarchical strategy does not weaken the engineering significance of the proposed model. On the contrary, the simplified wing model provides a verified aerodynamic-structural rapid evaluation module for the complete joined-wing model, and its correction strategy can be checked using CFD data. In this paper, aerodynamic and structural validation is completed based on the simplified single-wing model, while aerodynamic prediction for the simplified two-wing model is emphasized. The aerodynamic interference, load distribution and system-level geometric constraints of the full joined-wing configuration will be investigated in future work.

3. Establishment and Correction of the Aero-Structural Rapid Evaluation Model

3.1 Aerodynamic Rapid Evaluation Model

For the aerodynamic analysis, a VLM-based force prediction framework is first established for the simplified single-wing model. The VLM is a low-to-medium-fidelity aerodynamic method based on potential-flow theory. Its basic assumptions are that the perturbation flow around the wing is incompressible, inviscid and irrotational within the attached-flow regime. In the VLM, the wing is represented as a thin lifting surface and discretized into a set of vortex panels. Horseshoe vortices or vortex rings are placed on the lifting surface, as illustrated in Figure 2, to model the aerodynamic effect of the airfoil surface[3-5].

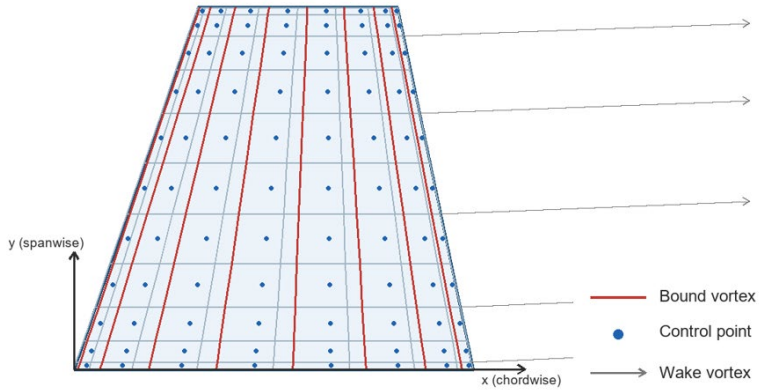


Figure 2 – Principle of the vortex lattice method

Based on potential-flow theory, the perturbation velocity potential in the VLM satisfies the Laplace equation, and the total velocity can be written as the sum of the freestream velocity and the perturbation velocity:

$$\nabla^2\phi = 0, \qquad V = V_\infty + \nabla\phi \tag{1}$$

The lifting surface is discretized into a finite number of vortex panels. For each panel, the bound vortex is placed at the quarter-chord line, the control point is placed at the three-quarter-chord line, and the trailing vortex extends downstream along the freestream direction. The induced velocity at a spatial point P generated by a finite straight vortex segment AB can be written using the Biot-Savart law as follows:

$$v_{AB}(P) = \frac{\Gamma}{4\pi}\frac{r_1 \times r_2}{|r_1 \times r_2|^2}\left[r_0 \cdot \left(\frac{r_1}{|r_1|} - \frac{r_2}{|r_2|}\right)\right] \tag{2}$$

where the vectors define the relative positions between the vortex-segment endpoints and the field point. For a horseshoe vortex consisting of one bound vortex segment and two trailing vortex segments, the induced velocity at control point P is the sum of the velocities induced by all vortex segments:

$$v = v_{bound} + v_{trail,L} + v_{trail,R} \tag{3}$$

The VLM requires the non-penetration condition to be satisfied at the control points. In the conventional formulation for a flat thin wing at small angles of attack, the non-penetration condition is usually simplified as a downwash balance in the global z direction, that is, only the vertical component of the induced velocity is used to cancel the vertical component of the freestream velocity:

$$\sum_{j=1}^{N} \Gamma_j w_{ij} = -V_\infty \sin\alpha_{eff} \tag{4}$$

This formulation is simple and is suitable for rapid evaluation of approximately planar wings during preliminary design. However, it implicitly assumes that the surface normal is approximately aligned with the global z direction. When sweep, camber, geometric twist or structural deformation exists, the actual panel normal can deviate significantly from the global z direction, and the simplified downwash condition cannot properly retain the sensitivity to effective angle of attack, sweep and twist.

In this paper, the complete local-normal boundary condition is adopted. Let the three-dimensional induced velocity generated at the i^{th} control point by the j^{th} unit-circulation vortex element be denoted by the corresponding influence coefficient, and let the local unit normal vector of the i^{th} panel be defined on the deformed surface. The non-penetration condition can then be written as:

$$\left(V_{\infty} + \sum_{j=1}^{N} \Gamma_j v_{ij} \right) \cdot n_i = 0 \tag{5}$$

$$A_{ij} = v_{ij} \cdot n_i, \qquad b_i = -f_a \left(V_{\infty,bc} \cdot n_i \right), \qquad A\Gamma = b \tag{6}$$

The local unit normal vector is obtained by taking the cross product of the local chordwise tangent vector, including the camber-line slope, and the spanwise tangent vector:

$$t_{c,i}^{*} = t_{c,i} + \left(\frac{dz_c}{dx} \right)_i | t_{c,i} | e_z, \qquad n_i = \frac{t_{c,i}^{*} \times t_{s,i}}{| t_{c,i}^{*} \times t_{s,i} |} \tag{7}$$

By solving the linear system in Eq. (6), the circulation of all vortex elements can be obtained. The aerodynamic force on each panel is then calculated using the Kutta-Joukowski theorem:

$$L = \rho V \Gamma \tag{8}$$

For the j^{th} bound vortex segment, the force can be written as:

$$dF_j = \rho \Gamma_j \left(V_{local,j} \times dl_j \right) \tag{9}$$

where the velocity is the sum of the freestream and induced velocities at the midpoint of the vortex segment, and the vector denotes the direction of the bound vortex segment. Projecting the aerodynamic force onto the lift and drag directions in the wind-axis system gives the lift and drag of the vortex panel:

$$L_j = dF_j \cdot e_L, \qquad D_j = dF_j \cdot e_D \tag{10}$$

Summing over all panels yields the total lift and drag of the wing:

$$L = \sum_{j=1}^{N} L_j, \qquad D = \sum_{j=1}^{N} D_j \tag{11}$$

For grid generation, a hybrid cosine distribution is used in both the spanwise and chordwise directions. The main part of the grid is based on uniform spacing, while cosine clustering is applied near the wing tip, leading edge and trailing edge where circulation gradients are large. This strategy avoids the excessive computational cost caused by globally dense grids. The general form of the cosine distribution is:

$$s(\mu) = \frac{1}{2} \left[1 - \cos(\pi \mu) \right], \qquad \mu \in [0,1] \tag{12}$$

Figure 3 shows the wing mesh generated by the hybrid cosine grid.

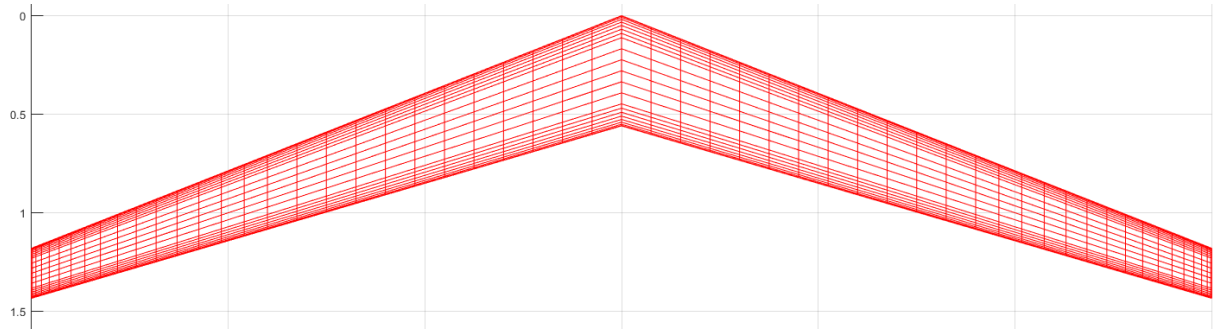


Figure 3 – Schematic of wing mesh generation

According to the preliminary design parameters of the front wing of the target aircraft, the parameters of the simplified single-wing model are set as shown in Table 1.

Table 1 – Aerodynamic design parameters

Parameter	Value	Parameter	Value
Span	6.0 m	Root chord	0.56 m
Tip chord	0.254 m	Leading-edge sweep angle	21.5°
Geometric twist angle	-2°	Maximum relative airfoil thickness	12%
Maximum airfoil camber	4%	Position of maximum camber	0.4c

The NACA4412 airfoil is selected as the wing-section shape. As a four-digit NACA airfoil, NACA4412 has a maximum camber of 4%, a maximum-camber position at 40% chord and a maximum relative thickness of 12%. The maximum camber, maximum-camber position and maximum relative thickness are used as the parametric description of the airfoil shape.

3.2 Corrections and Improvements for the Limitations of the VLM

3.2.1 Viscous Correction of Lift-Curve Slope

The VLM is based on potential-flow theory. When it is reduced to an infinite-span straight thin wing, the corresponding two-dimensional lift-curve slope differs from that of a real viscous airfoil. Therefore, under the design condition considered in this paper, namely an altitude of 1 km, a flight speed of 35 m/s, a mean aerodynamic chord of 0.407 m and a Reynolds number of approximately 0.9 million, the lift variation of the NACA4412 airfoil with angle of attack is calculated to obtain the viscous two-dimensional lift-curve slope. A viscous lift-curve-slope correction factor is then introduced, and the circulation equation becomes[5]:

$$A\Gamma = \kappa b \tag{13}$$

3.2.2 Drag Decomposition and Correction

The VLM can accurately predict circulation distribution, lift and induced drag, but it cannot directly model boundary-layer friction, viscous effects, pressure drag or separated stall. For low-speed flight, the total drag consists of induced drag and zero-lift drag[3,5]:

$$D_{total} = D_{induced} + D_{viscous} \tag{14}$$

The induced drag is calculated from the circulation using the Kutta-Joukowski theorem. Since the VLM cannot directly predict viscous drag and separation, a strip-theory correction is introduced to compute the sectional zero-lift drag. The zero-lift drag is decomposed into friction drag, pressure drag and separation drag:

$$D_{viscous} = \sum_{strip} qS_{strip}\left(C_{d,f,3D} + C_{d,p,3D} + C_{d,sep,3D}\right) \tag{15}$$

$$q = \frac{1}{2}\rho V_{\infty}^{2} \tag{16}$$

The friction drag is estimated using a turbulent flat-plate approximation, and the Hoerner form factor is used to account for airfoil-thickness effects:

$$C_f = \frac{0.074}{\mathrm{Re}^{0.2}} \tag{17}$$

$$FF = 1 + 2\frac{t}{c} + 60\left(\frac{t}{c}\right)^4 \tag{18}$$

$$C_{d,f} = 2C_f FF \tag{19}$$

where the parameter denotes the maximum airfoil thickness.

The pressure drag is represented by a combination of a quadratic term related to the local lift coefficient and an incidence-dependent drag term:

$$C_{d,p} = k_{profile}C_l^2 + K\sin^2\alpha \cdot f_{sweep} \cdot f_{fade} \tag{20}$$

The first term denotes the sectional profile-drag increment under lifting conditions: as lift increases, the pressure distributions on the upper and lower surfaces become asymmetric, and the suction peak, adverse pressure gradient and boundary-layer separation tendency are enhanced. Therefore, the two-dimensional airfoil drag polar is often approximated by a parabolic form. The second term represents incidence-related drag: as the angle of attack increases, the frontal projected area, leading-edge suction peak, separation tendency and pressure-recovery loss all increase. When the incidence angle is zero, this term vanishes. At small angles of attack it is approximately symmetric with respect to positive and negative angles, whereas at large angles it increases rapidly and approaches the trend of flat-plate pressure drag.

The zero-lift drag is calculated from sectional airfoil data and is therefore two-dimensional in nature. When it is extended to a three-dimensional wing, three-dimensional effects must be considered. For swept wings, the pressure distribution is influenced by spanwise flow. Therefore, pressure drag and additional separation drag are corrected for sweep effects in this paper, whereas friction drag is not corrected because it is less sensitive to sweep[10].

$$\begin{cases} C_{d,f,3D} = C_{d,fric,2D} \\ C_{d,p,3D} = \cos^3\Lambda \cdot C_{d,press,2D} \\ C_{d,sep,3D} = \cos\Lambda \cdot C_{d,sep,2D} \end{cases} \tag{21}$$

3.2.3 Stall and Post-Stall Correction

In the high-angle-of-attack separated-flow region, the conventional VLM continues to increase lift linearly according to the potential-flow solution, which leads to overpredicted lift and underpredicted drag. Although the optimization condition of the joined-wing aircraft in this study corresponds to a relatively small angle of attack, a simple correction is introduced to improve the generality of the aerodynamic rapid evaluation model. The Viterna-Corrigan post-stall polar is used to extrapolate sectional lift and drag[9-10]:

$$C_{l,post} = A_1 \sin(2\alpha) + A_2 \frac{\cos^2 \alpha}{\sin \alpha} \tag{22}$$

$$C_{d,post} = B_1 \sin^2 \alpha + B_2 \cos \alpha \tag{23}$$

The coefficients are determined from the lift and drag coefficients at stall and the equivalent drag coefficient at a 90 deg angle of attack. To avoid discontinuities, a smooth blending function is used to connect the pre-stall model with the post-stall model:

$$C = C_{base} + \eta\left(C_{post} - C_{base}\right), \qquad \eta = 3s^2 - 2s^3, \quad s \in [0,1] \tag{24}$$

For the positive-angle post-stall region, a small residual lift-retention term is also introduced to represent the weak vortex-lift retention that may exist after separation on swept wings:

$$\Delta C_{l,vortex} = G_v \sin^2 \alpha \cos \alpha \tag{25}$$

3.3 Structural Rapid Evaluation Model

For structural rapid evaluation, an equivalent beam model mainly reduces the wing to spanwise distributions of bending stiffness EI and torsional stiffness GJ. This approach is suitable for rapidly estimating the global bending deformation of high-aspect-ratio wings, but its structural degrees of freedom are primarily distributed along the span. It is therefore difficult to describe the two-dimensional stiffness distribution of the skin, spars, ribs and flange strips in the chordwise and spanwise directions, or to accurately represent local torsion, multiple load paths in the wing box and changes in the chordwise position of aerodynamic loads. In previous work, the equivalent beam model produced deflection errors of approximately 10% for some cases. If the single-beam model were still used in subsequent fluid-structure coupling and optimization, the structural approximation error would be propagated into the aerodynamic loads and optimization results.

Therefore, this paper advances from the equivalent beam model to the equivalent plate model. The wing box is treated as an orthotropic plate, and the contributions of the skin, spars, ribs and flange strips are included in the bending stiffness matrix D and transverse shear stiffness matrix As through stiffness equivalence. The equivalent plate model retains the two-dimensional stiffness characteristics of the wing box with relatively few degrees of freedom and can be regarded as a rapid structural analysis model between the equivalent beam model and high-fidelity shell/solid finite element models[8].

For the simplified single-wing model, the preliminary structural design parameters are selected as shown in Table 2.

Table 2 – Structural design parameters

Design parameter	Value	Design parameter	Value
Elastic modulus	71.7 GPa	Poisson's ratio	0.33
Front spar position	0.25c	Skin thickness	2 mm
Rear spar position	0.65c	Rib thickness	2 mm
Flange-strip thickness	0.01 m	Rib spacing	0.2 m

In the current model, the wing box is equivalent to an orthotropic plate. For each shared aerodynamic/structural panel, the equivalent wing-box height H is first estimated according to the local chord length, relative thickness and chordwise location. The stiffness contributions of the skin, ribs, spars and flange strips are then assembled into the element bending stiffness matrix D and transverse shear stiffness matrix As. The skin mainly contributes to bending stiffness and part of the torsional/shear stiffness through the distance of the upper and lower skins from the neutral plane. The ribs are converted into chordwise bending-stiffness contributions according to the rib spacing. The spars and flange strips mainly carry spanwise bending moments, so their chordwise positions have local effects on spanwise bending stiffness. This treatment preserves the explicit relationship between the structural design variables and the stiffness matrices, making it convenient to use skin thickness, rib spacing, rib thickness and flange-strip area as optimization variables. As shown in Figure 4, the spars are shown in red, the ribs in green and the skin in blue; the equivalent plate model converts these components into equivalent stiffness contributions.

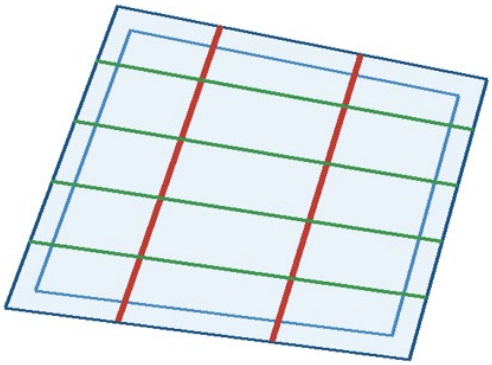


Figure 4 – Schematic of the equivalent plate model

The structural solution is obtained using a four-node Mindlin plate element. Each node contains three degrees of freedom: transverse deflection and rotations about the two in-plane axes. The Mindlin plate theory retains transverse shear deformation and is suitable for wing-box structures where the equivalent thickness is not negligible while computational efficiency must be maintained. The element stiffness consists of bending and shear terms. A 2 × 2 Gauss integration scheme is used for the bending term, and a 1 × 1 selective reduced integration scheme is used for the shear term to alleviate shear locking of low-order Mindlin plate elements in the thin-plate limit. The global structural equilibrium equation is[8]:

$$K_s u_s = f_s \tag{26}$$

where the stiffness matrix denotes the equivalent plate structural stiffness matrix, the displacement vector contains nodal deflections and rotations, and the load vector is obtained by mapping aerodynamic panel forces to structural nodes.

3.4 Bidirectional Fluid-Structure Coupling

The studied joined-wing aircraft operates at an altitude of 1 km and a flight speed of 35 m/s, with a Reynolds number of approximately 0.9 million. For the fluid-structure coupling problem, this condition can be regarded as a static aeroelastic problem. A quasi-static two-way coupled aerodynamic-structural rapid evaluation model is therefore constructed. To facilitate data transfer and reduce interpolation error, the aerodynamic and structural modules share the same mesh. The aerodynamic forces are obtained at the VLM control points, whereas the structural nodes are located at the four corners of each quadrilateral panel. In each coupling iteration, the aerodynamic model is first solved on the current deformed geometry to obtain panel forces. These aerodynamic loads are then mapped to structural nodes using the idea of four-node panel shape functions. After the structural solver obtains the deflection, the aerodynamic geometry is updated and the next aerodynamic solution is performed. When the change in the maximum deflection between two consecutive iterations satisfies a prescribed residual criterion, the two-way coupling is considered converged. The convergence criterion is:

$$\max_i \left| w_i^{(k)} - w_i^{(k-1)} \right| < \varepsilon \tag{27}$$

At the fluid-solid coupling interface, the coupled variables such as displacement and stress must be equal or conservative between the fluid and solid domains. The governing interface conditions are therefore written as:

$$n \cdot \tau_f = n \cdot \tau_s \tag{28}$$

$$r_f = r_s \tag{29}$$

where the stress and displacement variables are defined on the coupling interface, the vector denotes the outward unit normal, and the subscripts f and s denote the fluid and solid domains, respectively. In this work, a shared mesh and equivalent nodal-force mapping are used to transfer data between the aerodynamic and structural solvers[11].

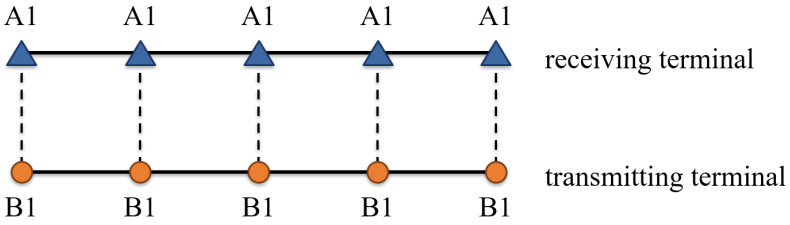


Figure 5 – Schematic of data transfer on the coupling interface

4. Hierarchical Validation of the Rapid Evaluation Model

4.1 Validation of Aerodynamic Predictions against CFD Data

The aerodynamic forces predicted by the two-way coupled aerodynamic-structural rapid evaluation model are compared with CFD data for the simplified single-wing model. The leading-edge sweep

angle is varied among 16.5 deg, 21.5 deg and 26.5 deg, and the angle of attack ranges from -10 deg to 18 deg. The comparisons are conducted at an altitude of 1 km under standard atmospheric conditions and a flight speed of 35 m/s, including lift, drag and lift-to-drag ratio.

Figure 6 shows the lift, drag and lift-to-drag-ratio curves of the simplified single-wing model with a 21.5 deg leading-edge sweep angle, comparing the rapid evaluation model with CFD data over the angle-of-attack range. The rapid evaluation model achieves high fitting accuracy for lift and drag between -10 deg and 10 deg. When the angle of attack exceeds 10 deg, the model still captures the trend of lift peaking and drag increasing rapidly due to flow separation. The lift-to-drag-ratio curve also indicates that the rapid evaluation model maintains high fitting accuracy and good robustness over different angles of attack.

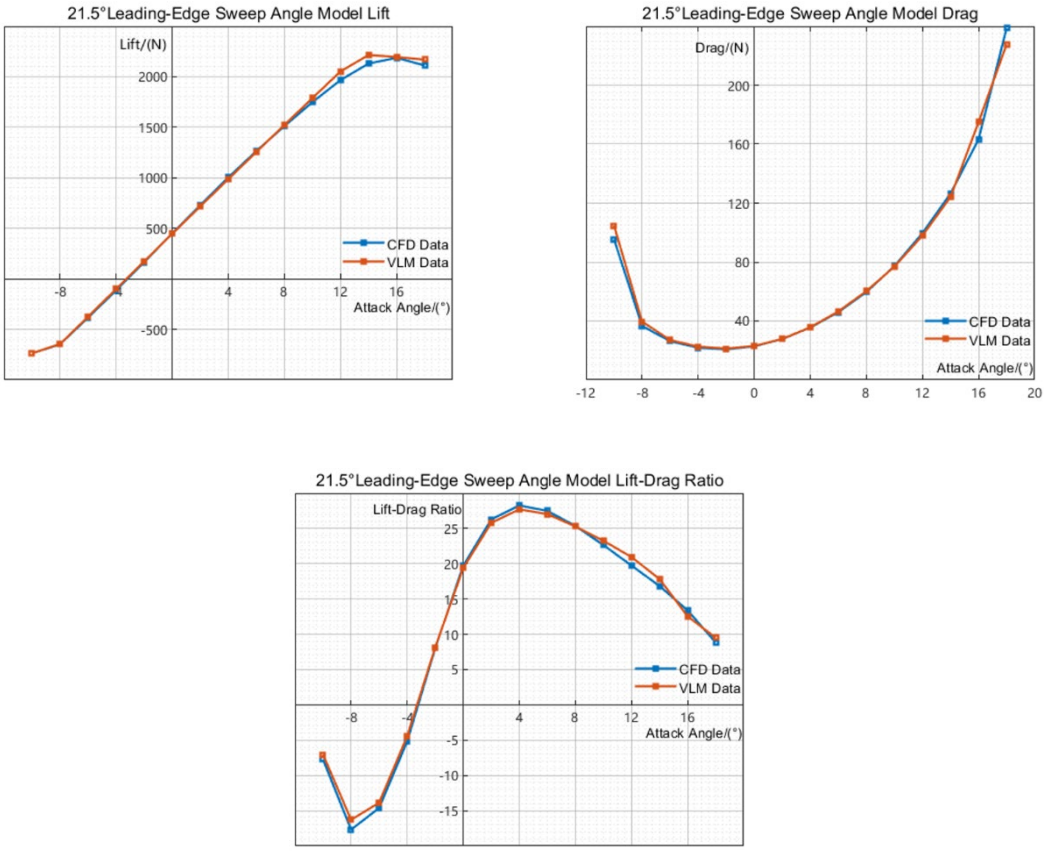


Figure 6 – Aerodynamic curves of the simplified single-wing model

Figure 7 presents the aerodynamic-error heat map of the simplified single-wing model for different leading-edge sweep angles. A relatively large lift error appears at an angle of attack of -4 deg because the lift is close to zero in this region. When the relative error is calculated, the small denominator amplifies the otherwise small absolute error. The large relative error of the lift-to-drag ratio at -4 deg originates from the same reason. The heat map clearly illustrates the error distribution between the rapid evaluation model and CFD data over different operating conditions. The relative errors of lift, drag and lift-to-drag ratio remain low in the angle-of-attack range from 0 deg to 8 deg, which satisfies the requirements of optimization-oriented preliminary design.



Figure 7 – Aerodynamic relative error heat map of the simplified single-wing model

4.2 Validation of Structural Deflection against FEM Data

The structural discipline is validated using the previously developed two-way coupled aerodynamic-structural rapid evaluation model. The maximum wing deflection predicted by the rapid evaluation model is compared with FEM simulation data. The comparison case is based on the simplified single-wing model with a 21.5 deg leading-edge sweep angle and a 4 deg angle of attack. The input loads for the FEM model are obtained from the wing-surface pressure files of the corresponding CFD simulation.

Figure 8 shows the maximum deflection and deformation predicted by the rapid evaluation model, whereas Figure 9 shows the maximum deflection and deformation obtained from the FEM simulation.

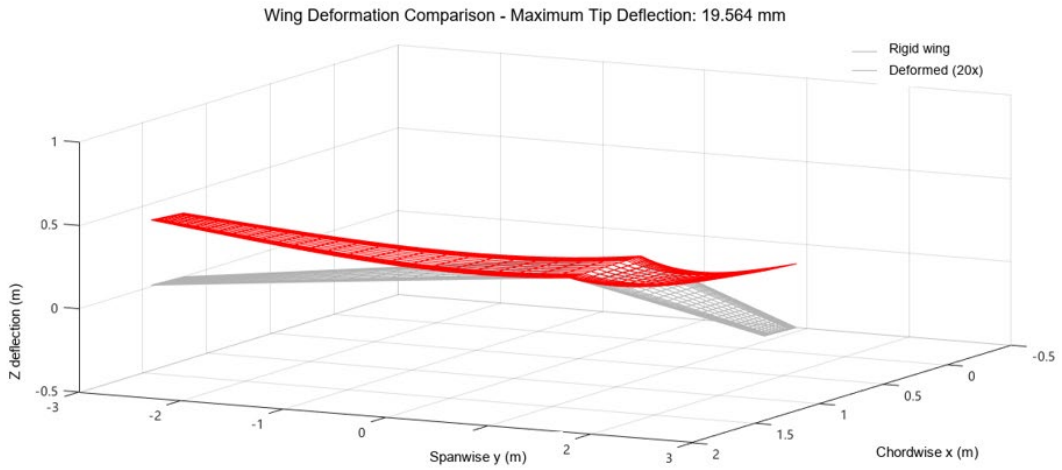


Figure 8 – Maximum deflection and deformation predicted by the rapid evaluation model

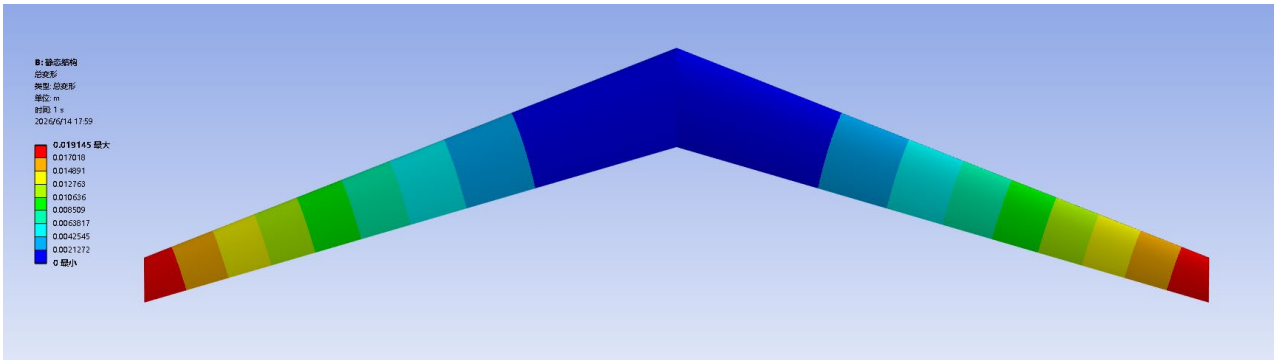


Figure 9 – Maximum deflection and deformation calculated by FEM

The maximum wing deflection predicted by the rapid evaluation model occurs at the wing tip and is 19.564 mm. The FEM simulation also indicates that the maximum deflection occurs at the wing tip, with a value of 19.145 mm. The relative prediction error is 2.2%, and the two deformation patterns are consistent. This demonstrates that the rapid two-way coupled aerodynamic-structural evaluation model predicts structural deflection with sufficient accuracy for optimization-oriented design.

5. Aerodynamic-Structural Multiobjective Optimization Based on NSGA-II

5.1 NSGA-II Multi-Objective Algorithm

NSGA-II is selected as the main algorithm for the subsequent aerodynamic-structural multi-objective optimization. NSGA-II is a multi-objective evolutionary algorithm based on non-dominated sorting, crowding-distance preservation and elitism. It can obtain a set of approximate Pareto-optimal solutions in a single optimization run without requiring the lift-to-drag ratio and structural weight to be artificially combined into a single weighted objective. For preliminary joined-wing design, the improvement of lift-to-drag ratio, reduction of structural weight, deformation control and geometric constraints are inherently conflicting. In addition, the objective functions may be nonlinear, locally non-smooth and

multimodal. Therefore, compared with gradient-based local optimization methods, NSGA-II imposes fewer requirements on differentiability and is more suitable for global exploration at the current stage[12-13,20-22].

In the proposed framework, NSGA-II is used only as an outer-loop optimizer that calls the rapid evaluation model. Each individual corresponds to a set of aerodynamic and structural design variables. The rapid evaluation model calculates responses such as lift, drag, lift-to-drag ratio, structural weight and maximum deflection, and the optimizer retains non-dominated solutions according to the objective functions and constraints. Since this paper focuses on the establishment and validation of the rapid evaluation model, the algorithmic details of NSGA-II are not expanded; the algorithm is used as an engineering optimization tool for obtaining the Pareto front.

5.2 Design Variables and Area Constraint

The design variables are divided into aerodynamic and structural variables. The aerodynamic variables include taper ratio, leading-edge sweep angle and geometric twist angle, which describe the wing planform, three-dimensional sweep effect and wing-tip unloading. The structural variables include skin thickness, rib spacing, rib thickness and flange-strip thickness, which control the bending stiffness, torsional stiffness and structural weight of the wing box. To prevent the optimization result from being dominated by lift increase due to a larger wing area, the wingspan and wing area are kept approximately constant during optimization. The root and tip chords are therefore re-parameterized using the taper ratio:

$$c_r = \frac{2S_{ref}}{b(1+\lambda)}, \qquad c_t = \lambda c_r \tag{30}$$

Accordingly, the optimization-variable vector is written as:

$$x = \left[\lambda, \Lambda_{LE}, \theta_{twist}, t_{skin}, L_{rib}, t_{rib}, t_{flange}\right]^T \tag{31}$$

The optimization variables and their ranges are listed in Table 3

Table 3 – Optimization design variables

Design parameter	Value
Taper ratio	[0.3, 1.0]
Leading-edge sweep angle / °	[10, 30]
Geometric twist angle / °	[0, 5]
Skin thickness / mm	[1, 4]
Rib spacing / m	[0.1, 0.5]
Rib thickness / mm	[1, 4]
Flange-strip thickness / mm	[5, 20]

5.3 Objective Functions and Constraints

A bi-objective formulation is adopted: under the constraints of required lift and structural deformation, the lift-to-drag ratio is maximized and structural weight is minimized. To allow a unified minimization form in NSGA-II, the maximization of lift-to-drag ratio is transformed into the minimization of the negative normalized lift-to-drag ratio:

$$\min F(x)=\left[-\frac{(L/D)(x)}{(L/D)_{ref}},\frac{W_s(x)}{W_{ref}}\right]^T \tag{32}$$

where the structural weight is estimated by the equivalent plate model, and the reference lift-to-drag ratio and structural weight are taken from the baseline configuration. The main constraints include the design-lift constraint, maximum-deflection constraint, area-preservation constraint and side constraints on design variables:

$$g_1(x)=1-\frac{L(x)}{L_{req}}\le 0 \tag{33}$$

$$g_2(x)=\frac{\delta_{\max}(x)}{\delta_{allow}}-1\le 0 \tag{34}$$

$$g_3(x)=\left|\frac{S(x)-S_{ref}}{S_{ref}}\right|-\varepsilon_S\le 0 \tag{35}$$

$$x_{\min}\le x\le x_{\max} \tag{36}$$

where the required lift is specified by the flight condition, the maximum deflection is obtained from the coupled structural calculation, the allowable maximum deflection is prescribed by structural requirements, and the area-preservation tolerance controls the variation in wing area. Individuals that violate the constraints can be removed or penalized using a feasibility-first rule during optimization.

5.4 Pareto-Front Generation and High-Fidelity Verification

NSGA-II produces a set of Pareto non-dominated solutions rather than a single optimum. For the aerodynamic-structural coupled optimization problem considered in this paper, the Pareto front represents the trade-off between improving the lift-to-drag ratio and reducing structural weight. Designs near the high-lift-to-drag side usually require stronger structural load-carrying capability and stricter deformation control, whereas designs near the low-weight side may sacrifice part of the aerodynamic efficiency or constraint margin. Representative solutions, including the maximum lift-to-drag-ratio point, minimum-weight point and compromise point, can be selected according to mission requirements. The compromise point can be identified using a knee-point criterion in the normalized objective space:

$$x_{knee}=\arg\min_{x\in\mathcal{P}}\left\|F_{norm}(x)-F_{ideal}\right\|_2 \tag{37}$$

After the Pareto front is obtained, several representative design points should be selected for high-fidelity verification. Aerodynamically, corresponding CFD models can be rebuilt to verify lift, drag, lift-to-drag ratio and load distribution. Structurally, corresponding FEM models can be established to verify maximum deflection, stress level and structural weight. If systematic discrepancies appear between

the high-fidelity simulations and the rapid evaluation model, the discrepancies can be fed back into the corresponding correction terms of the rapid model for further calibration. When high-fidelity samples are expensive to obtain, surrogate models or multi-fidelity residual models can also be used to improve the efficiency of design-space exploration[14,23].

6. Discussion and Future Work

The results indicate that the proposed two-way coupled aerodynamic-structural rapid evaluation model can achieve high prediction accuracy with limited samples. However, its applicability boundaries still need to be further clarified. First, the current validation object is a simplified single lifting surface and does not yet include the wake interference between the front and rear wings, end-plate interference or fuselage effects of the complete joined-wing configuration. Second, although the equivalent plate model has stronger two-dimensional stiffness representation capability than the equivalent beam model, its deflection and stiffness-equivalence accuracy should still be compared against FEM results for different configurations.

Future work will proceed in two directions. First, the prediction accuracy of the aerodynamic and structural disciplines should be validated for the simplified two-wing model and the complete joined-wing aircraft, with emphasis on front/rear-wing load distribution and aerodynamic interference. Second, aerodynamic-structural multi-objective optimization based on NSGA-II should be completed, and key design points on the Pareto front should be verified using high-fidelity simulations.

7. Conclusions

This paper develops a two-way coupled rapid evaluation framework based on a corrected vortex lattice method and an equivalent plate model to meet the demand for rapid and medium-fidelity aerodynamic-structural assessment during the preliminary design of joined-wing aircraft. Aerodynamically, the conventional VLM is extended by introducing a complete local-normal non-penetration boundary condition, hybrid cosine meshing and three-dimensional deformed-geometry modelling. Two-dimensional lift-curve-slope correction, drag decomposition, sweep-related drag correction and the Viterna-Corrigan post-stall model are introduced to compensate for the limitations of potential-flow methods in viscous drag and separation prediction. Structurally, the equivalent plate model is used to describe the contributions of the skin, spars, ribs and flange strips to the two-dimensional stiffness of the wing box, and quasi-static two-way coupling with aerodynamic loads is established. Validation based on the simplified single-wing model shows that the mean relative errors of lift, drag and lift-to-drag ratio over 45 CFD comparison cases are 2.69%, 3.45% and 5.29%, respectively, and the relative error of the maximum structural deflection compared with FEM is approximately 2.19%. These results demonstrate that the proposed model can satisfy the accuracy requirements for parameter screening and trend prediction in preliminary design. On this basis, an NSGA-II-based aerodynamic-structural multi-objective optimization framework with lift-to-drag ratio and structural weight as the core objectives is further constructed, providing a methodological basis for subsequent Pareto-front generation, high-fidelity CFD/FEM verification and model recalibration for the complete joined-wing configuration.

8. Acknowledgements

This work was supported by the Natural Science Foundation of Chongqing (Grant No. CSTB2023NSCQ-MSX0042). The authors would like to acknowledge the computing services from the Computing Center in Xi'an. The authors also sincerely thank the supervisors for their guidance on the research concept, model development and manuscript preparation, and thank the research-group members for their assistance in program debugging, simulation analysis and discussion of results.

9. Copyright Statement

The authors confirm that they, and/or their company or organization, hold copyright on all of the original material included in this paper. The authors also confirm that they have obtained permission, from the copyright holder of any third party material included in this paper, to publish it as part of their paper. The authors confirm that they give permission, or have obtained permission from the copyright holder of this paper, for the publication and distribution of this paper as part of the ICAS proceedings or as individual off-prints from the proceedings.

References

[1] Cavallaro R, Demasi L. Challenges, ideas, and innovations of joined-wing configurations: a concept from the past, an opportunity for the future. Progress in Aerospace Sciences, 2016, 87: 1-93.

[2] He C, Zhan F, Ma L, Chen G, Ma J. Aero-structural design of joined-wing aircraft based on high-fidelity model. Chinese Journal of Aeronautics, 2024, 37(4): 363-377.

[3] NASA. Vortex-lattice utilization. NASA Special Publication SP-405, 1976.

[4] Miranda L R, Elliott R D, Baker W M. A generalized vortex lattice method for subsonic and supersonic flow applications. NASA CR-2865, 1977.

[5] Katz J, Plotkin A. Low-speed aerodynamics: from wing theory to panel methods. 2nd ed. Cambridge: Cambridge University Press, 2001.

[6] Dagilis M, Kilikevicius S. Aeroelasticity model for highly flexible aircraft based on the vortex lattice method. Aerospace, 2023, 10(9): 801. doi:10.3390/aerospace10090801.

[7] Yang L, Xie C, Yang C. Geometrically exact vortex lattice and panel methods in static aeroelasticity of very flexible wing. Proceedings of the Institution of Mechanical Engineers, Part G: Journal of Aerospace Engineering, 2020, 234(3): 636-650.

[8] Vepa R. Aeroelastic analysis of wing structures using equivalent plate models. AIAA Journal, 2008, 46(5): 1216-1225.

[9] Viterna L A, Janetzke D C. Theoretical and experimental power from large horizontal-axis wind turbines. NASA TM-82944, 1982.

[10] Polhamus E C. Application of the leading-edge-suction analogy of vortex lift to the drag due to lift of sharp-edge delta wings. NASA TN D-4739, 1968.

[11] Farhat C, Lesoinne M, Le Tallec P. Load and motion transfer algorithms for fluid/structure interaction problems with non-matching discrete interfaces. Computer Methods in Applied Mechanics and Engineering, 1998, 157(1-2): 95-114.

[12] Martins J R R A, Lambe A B. Multidisciplinary design optimization: a survey of architectures. AIAA Journal, 2013, 51(9): 2049-2075.

[13] Deb K, Pratap A, Agarwal S, Meyarivan T. A fast and elitist multiobjective genetic algorithm: NSGA-II. IEEE Transactions on Evolutionary Computation, 2002, 6(2): 182-197.

[14] Paiva R M, Carvalho A R D, Crawford C, Suleman A. Comparison of surrogate models in a multidisciplinary optimization framework for wing design. AIAA Journal, 2010, 48(5): 995-1006.

[15] Wolkovitch J. The joined wing: an overview. Journal of Aircraft, 1986, 23(3): 161-178.

[16] Han Z, Long T, Song X, et al. Theory and method of aircraft multidisciplinary design optimization: current status and future direction. Aerodynamic Research & Experiment, 2024, 2(4): 26-57.

[17] Yao Y, Xu Y, Zhang Y, et al. Multidisciplinary optimization design of ultra-high altitude solar UAV. Journal of Nanjing University of Aeronautics & Astronautics, 2025, 57(3): 496-508.

[18] Afonso F, Vale J, Oliveira E, Lau F, Suleman A. A review on non-linear aeroelasticity of high aspect-ratio wings. Progress in Aerospace Sciences, 2017, 89: 40-57.

[19] Patil M J, Hodges D H, Cesnik C E S. Nonlinear aeroelasticity and flight dynamics of high-altitude long-endurance aircraft. Journal of Aircraft, 2001, 38(1): 88-94.

[20] Kenway G K W, Martins J R R A. Multipoint high-fidelity aerostructural optimization of a transport aircraft configuration. Journal of Aircraft, 2014, 51(1): 144-160.

[21] Gray J S, Hwang J T, Martins J R R A, Moore K T, Naylor B A. OpenMDAO: an open-source framework for multidisciplinary design, analysis, and optimization. Structural and Multidisciplinary Optimization, 2019, 59: 1075-1104.

[22] Martins J R R A. Aerodynamic design optimization: challenges and perspectives. Computers & Fluids, 2022, 239: 105391.

[23] Viana F A C, Simpson T W, Balabanov V, Toropov V. Metamodeling in multidisciplinary design optimization: how far have we really come? AIAA Journal, 2014, 52(4): 670-690.